JACS
JOURNAL OF THE AMERICAN CHEMICAL SOCIETY
Article
pubs.acs.org/JACS

Mechanistic Insight into DNA-Guided Control of Nanoparticle Morphologies

Li Huey Tan,[†] Yuan Yue,[‡] Nitya Sai Reddy Satyavolu,[†] Arzeena Sultana Ali,[†] Zidong Wang,[†] Yuqing Wu,[‡] and Yi Lu*[,†]

[†]Department of Chemistry, University of Illinois at Urbana−Champaign, Urbana, Illinois 61801, United States
[‡]State Key Laboratory of Supramolecular Structure and Materials, Jilin University, Changchun 130012, PR China

Supporting Information

ABSTRACT: Although shapes and surface characteristics of nanoparticles are known to play important roles in defining their properties, it remains challenging to fine-tune the morphologies systematically and predictably. Recently, we have shown that DNA molecules can serve as programmable ligands to fine-tune the morphologies of nanomaterials. Despite this discovery, the mechanism of how the morphology can be controlled and the roles of the DNA molecules in contributing to such control are not understood. We herein report mechanistic investigation of DNA-mediated morphological evolution of gold nanoprism seeds into nonagon, hexagon, and six-pointed stars, some of which display rough surfaces, in the presence of homo-oligomeric T30, G20, C30, and A30. The growth, elucidated through various analytical methods including UV−vis, SEM, TEM, zeta potential, fluorescence, and cyclic voltammetry, is found to occur in two stages: control of shape, followed by control of thickness. A careful analysis of diffraction patterns of the nanoprism seeds as well as the resulting intermediate shapes by TEM allowed us to deduce the exact sequence of shape evolution. Through systematic comparison of the nanoparticle growth process, the DNA molecules were found to play important roles by influencing diffusion of the Au precursor to the seed and modulating the growth through differences in DNA desorption, density, and mobility on the seed surface. These insights into the mechanism of DNA-guided control of nanomaterial morphologies provide deeper understanding of the interactions between the DNA and nanomaterials and will allow better control of the shapes and surface properties of many nanomaterials.

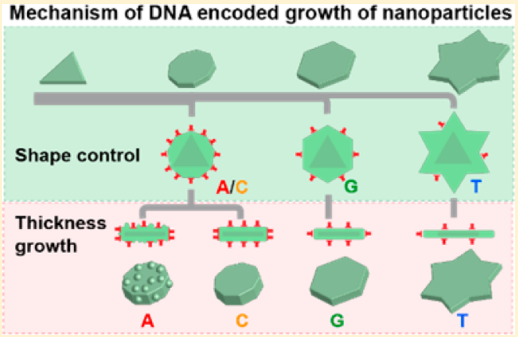

INTRODUCTION

It is well-established that most of the unique properties of nanoparticles (NPs), such as optical and catalytic properties, are derived from the NPs' morphologies, which include shape and surface characteristics.[1] Therefore, considerable efforts have been devoted toward controlling the NP morphologies.[2] Although numerous applications have taken advantage of the shape-dependent physical and chemical properties of NPs in applications such as in sensing, catalysis, and photonics,[3] it is a significant challenge to obtain synthesis methods that can rationally and deliberately control the morphology of NPs.[4] To meet this challenge, many studies have investigated the role of ligands (e.g., halides or small molecules such as citrate and cetyltrimethylammonium bromide) in controlling NP morphologies.[5] Despite this progress, it is still difficult to achieve systematic and predictive tuning of the NP morphologies because of limited fundamental understanding of the formation of NP morphologies and the mechanistic roles of these ligands.[6] There are many contradicting theories as to whether ligands play a thermodynamic or a kinetic role.[5b,7] Elucidation of the role of ligands is difficult because of wide variation in charge, size, and binding modes of ligands, making it difficult to perform comparable studies.

Recently, DNA has emerged as a promising "ligand" in controlling the NP morphologies because of its programmability that allows systematic variation of charge, size, hydrophobicity, and binding modes through the use of DNA with defined sequence and length.[2f,4,8] Through the nitrogen and oxygen functional groups on the nucleobases and sugar moiety as well as the electrostatic interactions of the phosphate backbone, the DNA has shown sequence-dependent affinity with gold,[2f,9] silver,[10] quantum dots,[11] and carbon NPs.[12] Taking advantage of these properties of DNA, we have recently reported the use of DNA oligonucleotides as programmable codes to control the growth of gold and silver NP seeds from either nanoprisms, nanocubes, or nanorods into various shapes with high uniformity in a sequence-dependent manner, allowing unprecedented fine control of NP morphologies.[13]

Although the above reports have demonstrated what DNA molecules can do to control the morphologies of nanomaterials, why each DNA sequence can result in different nanomaterial shapes and how they exert such a fine control is unknown.[14] With the ability to achieve fine control over the NP morphology, the DNA-mediated growth system is an ideal

Received: September 10, 2015
Published: October 22, 2015

DOI: 10.1021/jacs.5b09567
J. Am. Chem. Soc. 2015, 137, 14456−14464

system to study the growth mechanism and investigate the role of ligands to allow systematic and predictive control of the NP morphologies. Toward this goal, we report herein the mechanistic investigation of the growth of gold (Au) nanoprism seeds into different shapes and surface structures in the presence of homo-oligomeric adenine (A), thymine (T), cytosine (C), and guanine (G) under identical growth conditions. A two-stage growth mechanism was proposed on the basis of simultaneous monitoring and detailed analysis of the morphological evolution and plasmonic property changes. In addition, we have also elucidated the roles of DNA in the growth process through investigation of the influence of DNA on the Au precursor as well as investigation of the influence of DNA on the Au surface in terms of affinity, density, and mobility.

EXPERIMENTAL SECTION

Materials. All oligodeoxyribonucleotides were purchased from Integrated DNA Technologies (Coralville, IA). Hydrogen tetrachloroaurate(III) hydrate ($HAuCl_4$), hydroxylamine hydrochloride, sodium hydroxide, cetyltrimethlyammonium bromide (≥99%), sodium iodide, L-ascorbic acid, and sodium borohydride were purchased from Sigma-Aldrich.

Synthesis and Purification of Gold Nanoprisms. Gold nanoprisms were prepared using previously published procedures.[15] The as-prepared nanoprism solution was stored in a glass flask overnight to allow the nanoprisms to settle. Afterward, the supernatant was removed, and the gold nanoprisms were redispersed in 18.2 MΩ Millipore water (6−7 mL).

Synthesis of the Gold Nanoparticles Mediated by DNA.[13b] The freshly redispersed gold nanoprism solution was purified by centrifugation twice. Specifically, 700 μL of prism solution was concentrated via centrifugation for 2 min at 5900 rcf, the supernatant removed, and the pellet redispersed in 600 μL of Millipore water (18.2 MΩ). The solution was then centrifuged again and excess supernatant was removed. The pellet was again redispersed in 600 μL of Millipore water. There may be a small pellet still remaining at the bottom of the centrifuge tube, but only the particles that were resuspended readily were used in the next step. Formation of the pellet indicates that the majority of the cetyltrimethlyammonium bromide ligand was removed. The prism solution absorbance at 800 nm was then measured using an UV−vis spectrometer (Hewlett−Packard 8453), and adjusted by dilution to an absorbance of 0.7, which is ∼1 nM as determined from inductively coupled plasma mass spectrometry (ICP-MS). Typically, 100 μL of this solution was incubated with 2 μM of DNA for 15 min to allow the DNA to adsorb onto the gold nanoseeds. The amount of DNA added is approximately 2000 times excess from the seed concentration. NH_2OH (1 μL of 200 mM solution, adjusted to pH 5 with NaOH) was then added, and the solution was vortexed. $HAuCl_4$ (2.5 μL, 0.8% w/v) was then introduced to initiate the reduction reaction. A color change was observed in a few minutes, and the reaction was allowed to progress for at least 30 min. The reaction proceeded to completion when the gold precursor was mostly consumed and deposited on the NP seed, as confirmed from the ICP-MS determination of the gold concentration in the supernatant (Figure S1). For the phase plot to investigate DNA and gold concentration dependence, the concentrations of DNA and $HAuCl_4$ solutions were varied.

Monitoring Kinetics of the NP Growth. Mercaptopropionic acid (5 μL, 100 mM) was added to the growth solution at designated time points. The solution was charged with 10 μL 0.2% sodium dodecyl sulfate (SDS) before centrifugation for 2 min at 1500 rcf to purify the NPs. The particles were washed with water four times prior to imaging by SEM or TEM. SDS was added to prevent aggregation of the NPs in the first round of centrifugation when excess mercaptopropionic acid was present. Sonication was used whenever the particles formed pellets that were not readily dispersible.

Equipment and Characterization. The particles synthesized as well as the nanoassemblies formed were analyzed using a JEOL 2010LaB6/2100 cryo transmission electron microscope (TEM) operated at 200 kV or a Hitachi S4800 SEM with 10 kV and 10 μA. Kinetic UV−vis measurements were performed at 1 min intervals on a Cary 5000 UV−vis−NIR spectrophotometer.

RESULTS AND DISCUSSION

Simultaneous Monitoring of Morphological Evolution and Plasmonic Property Changes. The DNA-mediated growth of NPs was performed by first incubating 2 μM homo-oligomeric sequence of DNA (T30, G20, C30, or A30) with 100 μL of Au nanoprism seeds (100 nm in diameter and ∼7 nm in thickness) of ∼0.7 absorbance at 800 nm for 15 min, followed by addition of 2 mM hydroxylamine as reductant and 0.5 mM chloroauric acid as the Au precursor (Figure 1a). G20 was used instead of G30 because of the difficulties in synthesizing longer guanine oligonucleotides and formation of G quadruplex with longer G repeats.[16] To elucidate how the

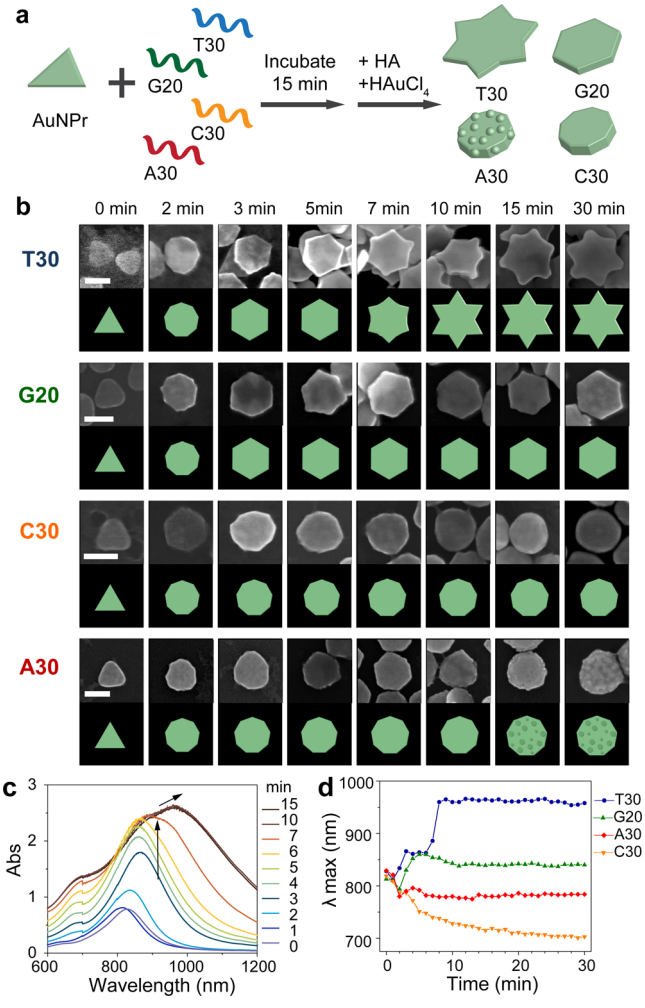

Figure 1. (a) Schematic representation of DNA-encoded growth of Au nanoprism seeds into four shapes using the four different DNA strands T30, G20, C30, and A30. (b) Enlarged SEM images showing representative images of the morphological evolution of Au nanoprisms prepared with T30, G20, C30, and A30 from 0 to 30 min with corresponding schematic images. Scale bars are 100 nm. (c) Kinetic UV−vis spectra of the T30-AuNP monitored at different time points. (d) λ_{max} values obtained from UV−vis spectra as in c, plotted versus time of AuNP growth in the presence of T30, G20, A30 and C30.

DOI: 10.1021/jacs.5b09567
J. Am. Chem. Soc. 2015, 137, 14456−14464

AuNP morphology evolves over time, we stopped its growth at different time points by adding a 400-fold excess of mercaptopropionic acid, which has been shown to bind the unreacted Au precursor and prevent further deposition of Au on the AuNP surface.[13b] The quenched AuNPs were purified from other components in the solution by centrifugation of the AuNP and washed with water four times. The morphological evolution of the AuNPs in the presence of T30, G20, C30, and A30 (hereafter called T30-, G20-, C30-, and A30-AuNP, respectively) were observed using SEM as shown in Figure 1b (large area view in Figure S2). In the presence of T30, the nanoprism seed first grew into a nonagon-shaped plate and then into an hexagonal shape, which persisted for 3−5 min (Figure 1b). At 7 min, pointed edges started to develop from the vertices of the hexagon, resulting in formation of a six-pointed star by 10 min, after which the shape did not change, though the AuNP did continue to grow larger.

Interestingly, the final shapes of the AuNPs grown in the presence of G20, C30, and A30 were intermediate shapes observed during the growth in the presence of T30 (Figure 1b). For example, the G20-AuNP transitioned through the same nonagon intermediate as in T30-AuNP and adopted its final hexagonal shape within 3−5 min, without going all the way to the six-pointed star. In contrast, A30-AuNP and C30-AuNP grew into nonagon shapes within 2−3 min and retained this shape throughout the growth duration. In addition to the shape changes, rough spots were observed to form on the surface of A30-AuNP around 15 min and became rougher with time.

In addition to monitoring the AuNP morphological evolution using SEM, we collected the UV−vis spectral changes of the growth solution in a parallel experiment (Figures 1c and S5a) because the absorbance of AuNPs and thus their plasmonic properties depends on the morphology and size.[17] To better elucidate the temporal changes in plasmonic properties of the AuNPs with the observed morphological transitions, we plotted the maximum absorbance wavelength (λ_{max}) of the growth of four oligonucleotide-AuNPs with time (Figure 1d). For T30-AuNP, the λ_{max} of the Au nanoprism, initially at 828 nm, blue-shifted to 812 nm in 1 min, consistent with the rounding of the particles,[18] and subsequently red-shifted to 866 nm at 3 min. It is interesting to note that the λ_{max} at 3−6 min remained almost constant but that the absorbance kept increasing during the same period (Figure 1c). This plateau in λ_{max} is consistent with persistence of the hexagonal shape observed in Figure 1b at 3−5 min. After 6 min, the λ_{max} continued to red-shift to 960 nm until 8 min and then remained constant. In addition to λ_{max} changes, the absorbance peak broadened at ∼7 min (Figure 1c), which corresponds to growth at the tips of the hexagon, indicating the beginning of the formation into six-pointed stars. Therefore, the UV−vis spectral changes correspond well with the morphological changes observed by SEM, where hexagon intermediates were observed at 3−5 min, before transitioning into six-pointed stars.

The UV−vis spectral changes of G20-, C30-, and A30-AuNP are shown in Figure S3b−d, and their λ_{max} changes with time are shown in Figure 1d. For the first 7 min, the λ_{max} of G20-AuNP followed a shift pattern similar to that of T30-AuNP. However, instead of further red-shifting of the λ_{max} as observed in T30-AuNP, the λ_{max} of G20-AuNP stopped changing. These results are consistent with G20-AuNP exhibiting the final hexagonal shape, which is an intermediate of T30-AuNP growth. In contrast, the λ_{max} of A30-AuNP blue-shifted in the first 3 min and remained relatively constant, whereas λ_{max} of C30-AuNP constantly blue-shifted slowly throughout the growth.

Analysis of the Shape Evolution. Considering that the above SEM images do not show direct in situ observation but instead depict snapshots of the AuNPs after addition of mercaptopropionic acid to stop the growth, the AuNPs formed in the intermediate stages need to be aligned with the original seed to allow analysis of the shape transition. Because the final shapes of the AuNPs grown in the presence of G20, C30, and A30 were intermediate shapes observed during the growth of T30-AuNP, we focused our analysis on the shape transformation of T30-AuNP. The selected area diffraction patterns, taken in the [111] zone axis for all of the NPs, contained the forbidden 1/3(422) reflections, which was consistent with the presence of twin planes even in the prism seed (Figure 2a−d). We aligned the intermediate shapes relative to the orientation of the prism seed by comparing the selected area diffraction pattern on each of the AuNPs (Figure 2a−d).

Upon identification of the orientation of the seed, the growth profile from the prism into the six-pointed star was elucidated. The growth from the prism occurred from the sides, outward in the direction of [11$\bar{2}$], [1$\bar{2}$1], and [$\bar{2}$11], forming a nine-sided

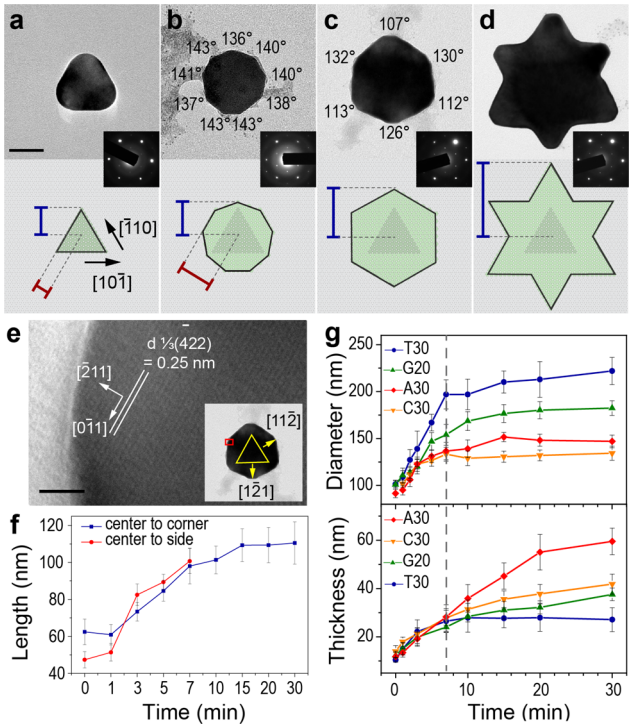

Figure 2. (a−d) TEM images showing progression of shape during transition from triangular prism seed to six-pointed star with corresponding model of the NP and diffraction pattern (insets). Scale bar is 50 nm. Blue and red lines on the models indicate the distance measured from the center to the corners or sides of the particles, respectively, plotted in f. (e) TEM image of the hexagonal T30-AuNP after 5 min of growth at high magnification. Scale bar is 2 nm. Red box shows the location where the higher-resolution image was observed. The lattice direction indicates the orientation of the seed as outlined by the yellow trace in inset. (f) Length of the T30-AuNP measured from the center to the corner (blue trace) and center to the side (red trace) with time, as defined in a−d. (g) Measured dimensions of the AuNPs at various time points during growth in the presence of T30, G20, A30 and C30 for diameter and thickness.

DOI: 10.1021/jacs.5b09567
J. Am. Chem. Soc. 2015, 137, 14456−14464

intermediate. Three sides were identified to originate from the prism seed, and six sides were newly formed, with two each at the vertices of the prism. The intermediate observed at 2 min had an average angle of 140°, consistent with the nonagon shape (Figure 2b). The growth continued in the six ⟨211⟩ directions to form hexagons and six-pointed stars. The hexagon intermediates formed at 5 min were found to have alternating larger (∼130°) and smaller (∼110°) angles with symmetry planes passing through the two opposite corners of the hexagon (Figure 2c). This observation is consistent with the growth of the sides of the prism and was no longer present in the hexagonal shape. The uneven contrast on the TEM images in Figure 2a may suggest an uneven surface or truncated edges on the surface of the particle. The presence of truncation is supported by further analysis of the hexagon shaped NP as shown in Figure S4.

This method of alignment using diffraction patterns had a 60° ambiguity because of the symmetry in the diffraction pattern. However, because the NPs slowly converged to be rather symmetrical with C6 rotation for the hexagon and six-pointed star in Figure 2c,d, the ambiguity of 60° is not as significant. More importantly, the conclusion of the observed growth of the NPs from the sides of the prism is still valid even with the 60° ambiguity. TEM at high magnification was used to identify the lattice patterns on the hexagon NP grown at 5 min. The d spacing observed corresponded well with the $^{1}/_{3}(\bar{4}22)$ reflection.[19] Upon analyzing the diffraction data, the lattice patterns were identified to be perpendicular to the $[\bar{2}11]$ direction and parallel to $[10\bar{1}]$ direction. This lattice direction is parallel to the edge of the prism, further affirming that the vertices on the prism seed were aligned with three of the vertices on the hexagon intermediate (Figure 2e, inset).

To determine the growth preference on the prism, we measured the length from the center of the AuNPs to the corners (defined by the blue line in Figures 2a−d) and the length from the center to the sides (defined by the red line in Figures 2a−d) at various time points. As shown in Figure 2f, the growth was faster initially from the sides, with a slope (red line) greater than that of growth from the corners (blue line) in the first 3 min. This difference in the growth rates suggests that the sides are favored for deposition of the Au precursor at these initial time points, resulting in rounding of the NP and thus formation of the nonagon shape. After 10 min, the growth rate subsequently became similar from both the corners and the sides. As a result, more symmetrical hexagons and six-pointed stars were formed.

To track the geometric growth progression of the AuNPs, the dimensions of the AuNPs grown at various time points are plotted in Figure 2g. The changes of the NPs diameters were similar in the presence of all four bases during the early growth period and reached a plateau or slowed down at ∼3 min for A30-AuNP and C30-AuNP, 5 min for G20-AuNP, and 7 min for T30-AuNP. From these time points onward, the AuNP shapes remained the same, and their diameters did not increase significantly with time. We noticed that the amount of time it took for the shapes of each oligonucleotide-AuNP to form correlates well with the binding affinity of the DNA bases to Au which is in the order of T < G < C < A.[9b] In contrast, the measured diameters of the particles at the end of growth were 220 ± 20 nm for T30-AuNP, 170 ± 10 nm for G20-AuNP, 155 ± 10 nm for A30-AuNP, and 129 ± 5 nm for C30-AuNP, which correspond well with the trend of observed λ_{max} values: T30-AuNP > G20-AuNP > A30-AuNP > C30-AuNP (i.e., larger AuNP displays larger λ_{max}). Although the binding affinity of A to Au is stronger than that of C, the diameter of the A30-AuNP is slightly bigger, attributable to the formation of rough surfaces on the A30-AuNPs.

In addition to shapes and sizes, the thickness of the particles was monitored, with A30-AuNP growing the thickest, followed by C30-AuNP and G20-AuNP, with the thinnest being T30-AuNP (Figure 2g). The order of AuNP thickness is an inverse of the diameter trend (e.g., while the thickness of T30-AuNP is the lowest, its diameter is the largest). In addition, while most of the changes in the AuNP diameters were completed within 7 min, their thickness grew at similar rates during the initial 7 min but started to grow at different rates after 7 min, depending on the homo-oligomeric strand used (Figure 2g). Comparing the changes in both thickness and diameter, we noticed two distinct steps, in which rapid growth in the diameter took place first, followed by an increase in the thickness. The final λ_{max} observed for each of the AuNPs grown in the presence of the four different sequences (Figure 1d) correlates well with the final diameter and thickness of the AuNPs (Figure 2g) because the more red-shifted λ_{max} is, the bigger the diameter but the smaller the thickness.[17] The plasmonic properties were consistent with the observed morphologies of the AuNPs, reaffirming the shape transition of the particle with time.

The deposition rate on the side of the Au nanoprism seeds may be enhanced because of the presence of reentrant grooves at the twin planes which are favorable for the attachment of adatoms.[20] For parallel {111} planes with multiple twins, the reentrant grooves where the deposition rapidly occurs are in the $[11\bar{2}]$, $[1\bar{2}1]$, $[\bar{2}11]$, $[\bar{1}12]$, $[\bar{1}2\bar{1}]$, and $[2\bar{1}\bar{1}]$ directions.[21] These six ⟨211⟩ directions correspond well with the directions of growth that we have observed on the sides of the nanoprism, suggesting the influence of stacking faults in the lateral growth. The different facets on the edges of platelike particles resulted in differing rates of growth in the lateral direction as observed by the enhanced growth with a sixfold symmetry in the ⟨211⟩ direction. To better analyze the rate of growth on the side with stacking faults and the top with {111} facets, the average change in diameter (measured in the direction of $[11\bar{2}]$) or thickness (measured in the direction of [111]) were obtained at two different time points. One of the time points was between 0 and 3 min for the onset growth rate, and another was between 10 and 20 min for the average growth rate after the initial onset but before the growth terminates. As summarized in Table S1, during the onset growth between 0 and 3 min, the rates of growth in the $[11\bar{2}]$ direction were much faster than that of growth in the [111] direction for all of the DNA bases. This increase in initial growth rate in the $[11\bar{2}]$ direction may be influenced by the presence of twin planes on the side of the particles that favor deposition. The growth rates began to change, however, in the middle of the growth from 10 to 20 min, by which time the rate of growth in the $[11\bar{2}]$ direction was faster than that in [111] for T30-AuNP and G20-AuNP but slower for C30-AuNP and A30-AuNP. The rate of growth for A30 between 10 and 20 min may be overestimated because the particles generated from A30 were rough. Despite this limitation, a general trend where the rate of growth in the $[11\bar{2}]$ direction decreases with increasing DNA binding affinity was observed, whereas the inverse trend was observed for the growth in the [111] direction. These results suggest that the bases with weaker binding affinity for Au (e.g., T) would favor the growth to form {111} facets, resulting in particles with larger {111} surface area. In contrast, the bases with stronger

DOI: 10.1021/jacs.5b09567
J. Am. Chem. Soc. 2015, 137, 14456−14464

binding affinity for Au (e.g., A) would better bind to the side facet of the particle containing stacking faults, as compared to the {111} facets, resulting in faster deposition of Au on the {111} surface and thus thicker particles. The growth rates on the side of the NP at the later time points correlated well to the presence and preferential binding of DNA. The observation of a significant decrease in growth of the diameter while the thickness continues to grow is rather interesting. Similar observations of significant decrease in the growth rate of one facet while the other facet continues to grow have been made recently in a study of the growth of platinum nanocubes using in situ TEM.[22] The arrested growth of the {100} facet was attributed to a kinetically controlled growth instead of thermodynamically controlled growth.

Roles of the DNA in the Morphological Evolution. A critical question is the role of DNA in controlling the morphological evolution of AuNPs. To ensure that the growth is mainly affected by DNA, we first need to confirm that the growth in the presence of 2 mM hydroxylamine as reductant is rate-independent.[5b] The particle growth was tested at various reductant concentrations, and we found no change in NP shape for reductant concentrations below 2 mM (Figure S5). At concentrations higher than 2 mM, the growth was inhomogeneous (Figure S6), suggesting a rapid and diffusion-limited reduction process.[23] Therefore, the 2 mM reductant concentration used in our studies was ideal to ensure slow reduction and to allow DNA to control the growth.

In principle, the ease of Au precursor deposition on AuNP can be influenced by DNA through (1) the binding of DNA to the Au precursor, (2) the ease of DNA dissociation from the AuNP, (3) the density of DNA on the AuNP surface, and (4) the mobility of the DNA on the AuNP surface. The first factor, the DNA binding to the precursor, can influence either the reduction potential of Au and therefore the reduction rate or the diffusion of Au precursor to the AuNP surface. To investigate the exact role, cyclic voltammetry (CV) of the Au precursor in the presence of the four different DNA sequences was performed on an Au electrode using Ag/AgCl as a reference electrode. The results showed no significant change in the reduction peak potentials, but the cathodic current decreased with different DNA bases in the order of T > G > C > A, which is similar to the binding affinity of DNA to Au (Figure S7). To investigate if this diffusion rate is the main criteria that influences the AuNP growth, we correlated the rate of diffusion from our CV data with the rate of change in volume of each particle. We found that the relative volume change was higher than the relative rate of diffusion between the different DNA strands (see more explanation in the Supporting Information). Hence, although the diffusion of the precursor may influence the growth, other factors such as the presence of a twin plane on the NP can influence the rate as well. The diffusion of gold precursor measured by CV applies to the {111} surface, but the rate of diffusion of the precursor in the presence of different DNA strands may change depending on the facet of gold. These results indicate that the DNA molecules do not influence the reduction potential of the Au precursor; instead, they influence the diffusion of the Au ion to the Au electrode surface, as evidenced by the different cathodic currents observed. The second factor, the ease of DNA dissociation from the AuNP, is related to the binding affinity of the DNA. The effect of DNA binding affinity to Au in the order of T < G < C < A[9b] has been demonstrated in our study above to influence the shape of the NP.

The third factor was investigated on the basis of the DNA concentration on the NP. To measure the DNA density on the AuNP surface, we quantified the number of DNA molecules on the AuNPs, using A30 and T30, which have the strongest and weakest binding affinities, respectively,[9b] as representative cases. Fluorophore-labeled A30 and T30 were used in the AuNP growth process (Figure S8). Upon removal of excess DNA and etching of the AuNP, the number of DNA on each particle after growth was determined from fluorescence measurements (Figure S9). The number of T30 DNA on the T30-AuNP (23 ± 2) is about 10 times less than the number of A30 DNA (240 ± 50) on the A30-AuNP. As a result of the dynamic nature of the DNA binding to the AuNPs, this method of measuring DNA on the AuNPs after removing the excess DNA provided only an estimate. Because we used the same method to measure the amount of DNA for all nucleotides and because the mechanistic investigations in this work relied on relative binding properties of the four nucleotides, any systematic error due to the method of measurement had minimal effect on the conclusions drawn from this work. On the basis of the total surface area per particle of 7.46×10^{-14} m^2 for A30-AuNP and 8.13×10^{-14} m^2 for T30-AuNP, the minimal DNA densities on the particles were calculated to be approximately one A30 strand per 3.1×10^2 nm^2 area and one T30 strand per 3.5×10^3 nm^2 area. Hence, the density of A30 on the particle is about 10 times more than that of T30. These results were consistent with the zeta potential measurements because the $+37 \pm 1$ mV measurement for CTAB-coated nanoprism became more negative for A30-AuNP (-36 ± 1 mV) than for T30-AuNP (-19 ± 2 mV). Both results indicate that the higher-affinity A30 oligonucleotide resulted in higher DNA density on the Au surface.

Since the density of DNA on the AuNP plays a role in influencing the AuNP morphology, we wondered if the DNA density could be increased by increasing the DNA concentration during the growth stage, even for the DNA oligonucleotides with weak affinity. To answer this question, the growth of AuNP in the presence of different concentrations of T30 (the DNA with the weakest affinity to Au) and Au precursor ($HAuCl_4$) was investigated, and the resulting AuNP shapes were plotted in a phase diagram, showing growth into four categories of shapes (round, hexagonal, six-pointed star, and irregular overgrown particles; Figure 3a). When the concentrations of T30 and $HAuCl_4$ were low, as shown by the gray area on Figure 3a, the undergrown particles with round shapes were observed (Figure 3b1,c1). At very high $HAuCl_4$ concentration (red area on Figure 3a), the AuNPs were overgrown and lost their regularity in shape (Figure 3c4,c5) because of fast and uncontrolled AuNP growth. The formation of the final six-pointed star shape occurred only at certain DNA and $HAuCl_4$ concentrations (blue region on Figure 3a). Interestingly, high T30 concentrations but low concentrations of $HAuCl_4$ (green area on Figure 3a) resulted in AuNPs with hexagonal shape, which is similar to the final shape formed by G20-AuNPs (Figure 3b4,b5).

To elucidate further the effect of DNA concentration on the growth, we compared the dimensions of the AuNPs by measuring their diameter and thickness from SEM micrographs. With increasing concentrations of T30, the diameter of the AuNP became smaller, but the thickness increased (Figure 4a). Comparing the six-pointed star AuNPs that were grown in the presence of 0.5 mM of $HAuCl_4$ and increasing concentrations (2, 5, 10, and 15 μM) of T30, the lateral dimensions decreased

DOI: 10.1021/jacs.5b09567
J. Am. Chem. Soc. 2015, 137, 14456−14464

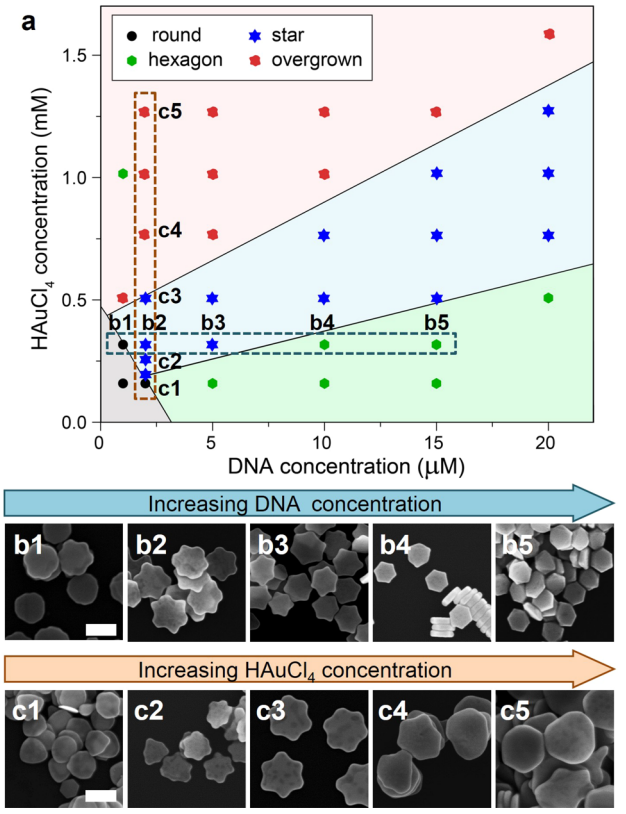

Figure 3. (a) Phase diagram for different shapes of AuNPs obtained when nanoprism seeds were grown at a range of T30 DNA concentrations from 1 to 20 μM and $HAuCl_4$ concentrations from 0.19 to 1.9 mM. Each shape in the plot is determined experimentally. SEM micrographs at the bottom are representative of the samples indicated in the phase diagram with (b) increasing T30 concentration at a constant concentration (0.32 mM) of $HAuCl_4$ and (c) increasing $HAuCl_4$ concentration at a constant concentration (2 μM) of T30. All of the NPs were grown for at least 2 h until the precursor was fully depleted. Scale bars are 200 nm.

from 280 ± 20 to 260 ± 30, 190 ± 10, and 170 ± 5 nm, respectively. At the same time, the thickness increased from 20 ± 4 to 34 ± 4, 36 ± 6, and 49 ± 7 nm, respectively. In contrast, changing the $HAuCl_4$ concentration increased the diameter of the AuNP but had minimal effect on the thickness (Figure 4b). These observations where the thickness was independent of the gold concentration but diameter was dependent on the gold concentration suggest that the rate-limiting step was the diffusion of the gold precursor to the fast-growing edge facets. The effect of increasing the DNA concentration that limited the lateral growth was similar to the effect of increasing the DNA binding affinity and thus affected the diffusion of the precursor to the NP seeds. Increasing the concentration of T30 by 10 times (from 2 to 20 μM) did not result in the change of NPs shape of T30-AuNP to that of A30-AuNP. The higher DNA concentration, however, did limit the growth to the hexagon-shaped NPs, similar to particles grown in the presence of G20. These results suggest that both the binding affinity and concentration of DNA play vital roles in controlling the rate of growth and influencing the final NP shapes.

The fourth factor, the mobility of DNA on the Au surface, can influence the particle roughness. A30 DNA was the only oligonucleotide to result in formation of particles with rough surfaces, which was observed only between 10 and 15 min of growth. Diffraction on the particle formed by A30-AuNP on the [111] zone axis shows multiple diffraction patterns, suggesting that the roughness is due to new nucleation sites on the NP (Figure S10). The mobility of nucleobases on the Au{111} surface was previously reported to be in the order of A < G ≈ T < C,[24] which is different from the order of DNA affinity. The DNA mobility on the Au surface is not related to the binding affinity but is instead driven by the number of anchor points and the exchange of position caused by mismatch of the distances of binding sites between the base and the Au lattice.[24] This result explains the observation that although both C and A have high binding affinity, C30-AuNP has a smooth surface whereas A30-AuNP displays a rough surface. The low mobility of A30 forces the Au precursor to deposit at regions where the DNA does not bind, thereby resulting in a rough particle. In

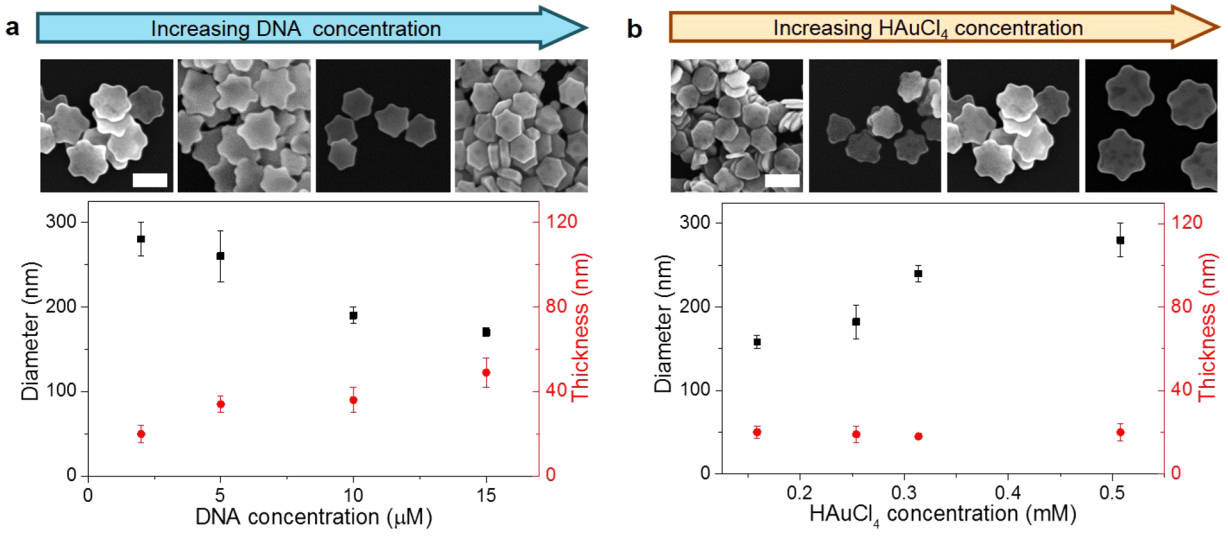

Figure 4. Graph showing the diameter and thickness of the T30-AuNPs measured from SEM micrographs (a) varying DNA concentrations at constant concentration (0.5 mM) of $HAuCl_4$ and (b) varying $HAuCl_4$ concentrations at constant concentration (2 μM) of T30. Representative SEM images of each sample are shown above each graph. All of the NPs were grown for at least 2 h until the precursor was fully depleted. Scale bars are 200 nm.

DOI: 10.1021/jacs.5b09567
J. Am. Chem. Soc. 2015, 137, 14456−14464

Scheme 1. Proposed Mechanism of Growth of Au Nanoprisms Influenced by DNA in Two Stages: Shape Control and Thickness Growth

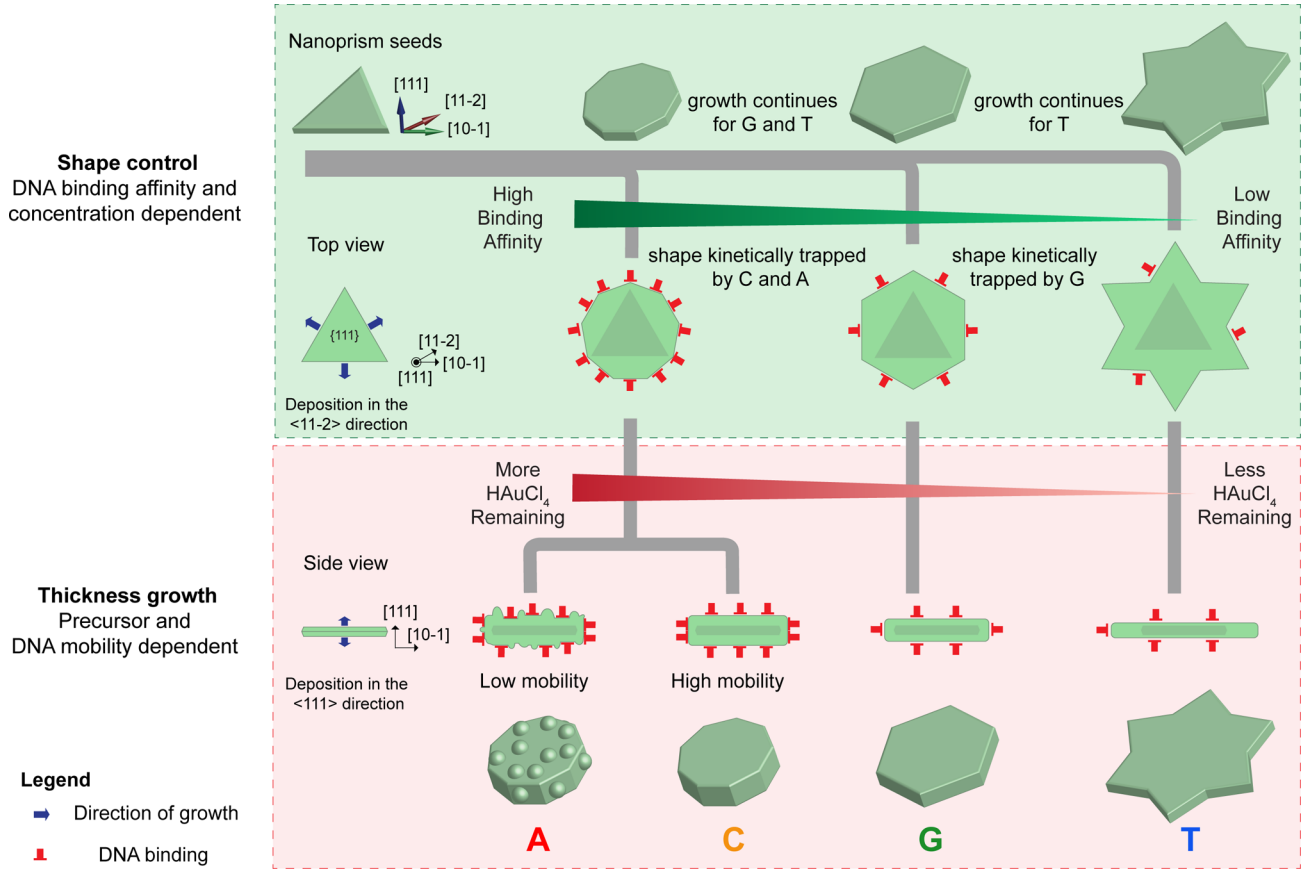

contrast, because C30 has high mobility, it allows for even deposition of Au. The role of DNA in preventing the deposition of Au precursor on the seed was demonstrated by using 5 nm AuNP functionalized with the complementary DNA sequence to probe the position of DNA A30 on the rough particle (Figure S11, further explanation available in the Supporting Information). The 5 nm AuNPs were observed to hybridize mainly at the crevices of the rough features, consistent with DNA binding and thus hindering the Au deposition. This observation is also consistent with previous observations of the overgrowth of Au on DNA-coated AuNPs, where polycrystalline growth was observed.[8b,c]

Proposed Mechanism. To describe the mechanism of the AuNP morphological evolution, the growth is divided into two stages (Scheme 1). In the first stage, the AuNP shapes are controlled by the binding affinity of DNA on the AuNPs and the concentration of DNA used during the growth process. The binding of ligands on Au is a reversible process with the equilibrium dependent on the binding affinity and concentration of the ligand.[25] When the DNA concentration in the solution was the same for each DNA, the effect of DNA binding affinity was observed. The nanoprisms can grow through nonagon and hexagon intermediates to form six-pointed stars in the six directions guided by the reentrant grooves from the twin planes. The evolution of the nanoprism to the final shape depends on the DNA binding affinity. The DNA binding affinity affects the ability of the DNA to desorb from the surface, making it difficult for Au to deposit at locations to which DNA can bind. In Scheme 1, the relative density of DNA bound on each particle is represented as the relative number of red binding arrows depicted. Therefore, the bases with higher affinity (A and C, with more red arrows) can kinetically trap the AuNPs at the nonagon shape during the early stage growth, whereas a base with a weaker affinity (G, less red binding arrows) could trap the shape only at a later stage of the growth (i.e., hexagon). Because T has the weakest affinity, it allows growth all the way to six-pointed stars. Additional support for this mechanism comes from varying the DNA concentration. In the presence of higher concentrations of T30, instead of growth into a six-pointed star, the hexagon was observed as the final shape. Despite T30 having the lowest affinity, the higher T30 concentration can increase the DNA density on the gold surface, thereby hindering gold deposition and trapping the growth at the hexagonal shape, as observed with G20, which has a higher binding affinity. In our investigation of the preference of DNA growth on different facets of the AuNPs, the discussions focus mainly on DNA binding to the Au{111} because most reports so far are limited to this facet.[9a,b] Despite this limitation, our observation that the DNA sequences with stronger binding affinity are capable of stabilizing higher-energy facets to prevent the sides from growing is consistent with those from the growth of gold on other seeds, such as Au nanorods, where the higher energy facets on the sides of the nanorod is blocked from growth by stronger-binding-affinity bases such as A.[13d] The efficiency in hindering the growth of the higher energy sides were even more evident for phosphorotioate-modified DNA A30 that has even stronger binding affinity.[13d]

DOI: 10.1021/jacs.5b09567
J. Am. Chem. Soc. 2015, 137, 14456−14464

After the AuNP shapes are formed, the second stage occurs in which new growth is primarily in the thickness of the AuNP (Scheme 1 and Figure 2g). The thickness change depends on the amount of remaining Au precursor in the solution after the shape has formed, which is inversely related to the diameter of the NP. The thickness remained almost constant for T30-AuNPs after 7 min because the Au source had been depleted as a result of formation of AuNPs with large diameters. However, the G20-, C30-, and A30-AuNPs continued to grow thicker because the diameter of their AuNPs were smaller; thus, more Au was still available for deposition, resulting in an inverse relationship between the diameter and thickness of the AuNPs (Figure 2g). However, although the amount of Au remaining for A30 and C30 is similar, the surface morphology is different. The AuNP roughness depends on the DNA mobility on the Au{111} surface. The low mobility of A30 drives the deposition of Au on locations where DNA is not bound, resulting in a rough surface. In contrast, despite the high binding affinity, the higher mobility of C30 on Au{111} permits an even deposition of Au on the Au{111} surface. We hypothesize that the location of DNA bound to the particle might be different for the side or for the top surface, which subsequently influences the growth of the particle in the [111] and [11$\bar{2}$] direction depending on the DNA sequence.

CONCLUSIONS

We have investigated the mechanism of DNA-mediated NP growth from Au nanoprism seeds into four different shapes and provided an in-depth study of the role of different homo-oligomeric DNA sequences (e.g., A30, T30, G20, and C30) in controlling the NP morphologies. The morphological evolution observed by SEM and TEM correlates well with the plasmonic properties of the NPs monitored by UV−vis. The T30-AuNPs grow from nanoprisms to nonagons, followed by hexagons, and finally six-pointed stars. Interestingly, the final shapes in the presence of other DNA oligomers match the intermediates observed for T30-AuNP, such as nonagons (for A30-AuNP and C30-AuNP) and hexagons (for G20-AuNP). The mechanism for the growth of the nanoprisms by DNA is proposed to occur via two stages: first, growing into different shapes, and second, growing in thickness.

DNA influences the growth of AuNPs by surface passivation and kinetically hindering the deposition of Au. The role of DNA is demonstrated through its influence on the diffusion of Au precursor to the Au surface through the ease of DNA desorption from the Au surface and through the DNA density and mobility on the Au surface. The ability of DNA to dissociate from the Au surface is related to the binding affinity of the DNA bases to Au, whereas the DNA density would depend on the binding affinity of the DNA base and on the concentration of DNA in solution. As a result, a strong correlation can be made between the binding affinities of the DNA bases toward Au (in the order of T < G < C < A) and the final shapes of the resulting AuNPs. Although both A and C have high binding affinity to Au, A has lower mobility on the Au{111} surface in comparison to that of C, resulting in deposition of Au in locations where the DNA did not bind, thus forming a rough surface. In contrast, the high mobility of C allows for even deposition of Au and thus results in a smooth surface.

Having identified the origin and mechanism for such fine control offered by DNA, this study offers a deeper understanding of ligand-mediated control of NP growth and allows for the development of methods for the formation of a variety of shapes and surface properties in a more predictable manner.

ASSOCIATED CONTENT

Supporting Information

The Supporting Information is available free of charge on the ACS Publications website at DOI: 10.1021/jacs.5b09567.

Additional experimental procedures, notes on the position of DNA on the particle, and additional supporting figures of SEM and TEM images. (PDF)

AUTHOR INFORMATION

Corresponding Author

*yi-lu@illinois.edu

Notes

The authors declare no competing financial interest.

ACKNOWLEDGMENTS

We thank Dr. Parisa Hosseinzadeh, Dr. Hang Xing, Dr. Tingjie Song, Dr. Longhua Tang, Yin Liu, Dr. Jianbo Wu, and Prof. Catherine Murphy for insightful discussions. We also thank Kevin Hwang and Ryan Lake for help with proofreading. L.H.T. was supported at UIUC from NIH National Cancer Institute Alliance for Nanotechnology in Cancer "Midwest Cancer Nanotechnology Training Center" Grant R25 CA154015A. SEM and TEM were carried out at the UIUC Materials Research Laboratory.

REFERENCES

(1) (a) Scholl, J. A.; Koh, A. L.; Dionne, J. A. *Nature* **2012**, *483*, 421. (b) Murphy, C. J.; Sau, T. K.; Gole, A. M.; Orendorff, C. J.; Gao, J.; Gou, L.; Hunyadi, S. E.; Li, T. *J. Phys. Chem. B* **2005**, *109*, 13857. (c) Burda, C.; Chen, X.; Narayanan, R.; El-Sayed, M. A. *Chem. Rev.* **2005**, *105*, 1025.

(2) (a) Yin, Y.; Alivisatos, A. P. *Nature* **2005**, *437*, 664. (b) Tao, A. R.; Habas, S.; Yang, P. *Small* **2008**, *4*, 310. (c) Xia, Y.; Xiong, Y.; Lim, B.; Skrabalak, S. E. *Angew. Chem., Int. Ed.* **2009**, *48*, 60. (d) Langille, M. R.; Personick, M. L.; Mirkin, C. A. *Angew. Chem., Int. Ed.* **2013**, *52*, 13910. (e) Zhao, P.; Li, N.; Astruc, D. *Coord. Chem. Rev.* **2013**, *257*, 638. (f) Tan, L. H.; Xing, H.; Lu, Y. *Acc. Chem. Res.* **2014**, *47*, 1881.

(3) (a) Haruta, M. *Catal. Today* **1997**, *36*, 153. (b) Liu, J.; Lu, Y. *J. Am. Chem. Soc.* **2003**, *125*, 6642−6643. (c) Hu, M.; Chen, J.; Li, Z.-Y.; Au, L.; Hartland, G. V.; Li, X.; Marquez, M.; Xia, Y. *Chem. Soc. Rev.* **2006**, *35*, 1084. (d) Lal, S.; Clare, S. E.; Halas, N. J. *Acc. Chem. Res.* **2008**, *41*, 1842. (e) Anker, J. N.; Hall, W. P.; Lyandres, O.; Shah, N. C.; Zhao, J.; Van Duyne, R. P. *Nat. Mater.* **2008**, *7*, 442. (f) Huang, X.; Neretina, S.; El-Sayed, M. A. *Adv. Mater.* **2009**, *21*, 4880. (g) Liu, J.; Cao, J.-H.; Lu, Y. *Chem. Rev.* **2009**, *109*, 1948−1998. (h) Wang, F.; Han, Y.; Lim, C. S.; Lu, Y.; Wang, J.; Xu, J.; Chen, H.; Zhang, C.; Hong, M.; Liu, X. *Nature* **2010**, *463*, 1061. (i) Zhao, W.; Chiuman, W.; Lam, J. C. F.; McManus, S. A.; Chen, W.; Cui, Y.; Pelton, R.; Brook, M. A.; Li, Y. *J. Am. Chem. Soc.* **2008**, *130*, 3610. (j) Wu, P.; Hwang, K.; Lan, T.; Lu, Y. *J. Am. Chem. Soc.* **2013**, *135*, 5254−5257. (k) Torabi, S.-F.; Lu, Y. *Curr. Opin. Biotechnol.* **2014**, *28*, 88−95.

(4) Sun, W.; Boulais, E.; Hakobyan, Y.; Wang, W. L.; Guan, A.; Bathe, M.; Yin, P. *Science* **2014**, *346*, 1258361 DOI: 10.1126/science.1258361.

(5) (a) Ji, X.; Song, X.; Li, J.; Bai, Y.; Yang, W.; Peng, X. *J. Am. Chem. Soc.* **2007**, *129*, 13939. (b) Personick, M. L.; Mirkin, C. A. *J. Am. Chem. Soc.* **2013**, *135*, 18238. (c) Mourdikoudis, S.; Liz-Marzán, L. M. *Chem. Mater.* **2013**, *25*, 1465. (d) Garg, N.; Scholl, C.; Mohanty, A.; Jin, R. *Langmuir* **2010**, *26*, 10271. (e) Lohse, S. E.; Murphy, C. J. *Chem. Mater.* **2013**, *25*, 1250.

(6) (a) Nikoobakht, B.; El-Sayed, M. A. *Langmuir* **2001**, *17*, 6368. (b) Slocik, J. M.; Naik, R. R. *Chem. Soc. Rev.* **2010**, *39*, 3454.

(c) Bealing, C. R.; Baumgardner, W. J.; Choi, J. J.; Hanrath, T.; Hennig, R. G. *ACS Nano* **2012**, *6*, 2118. (d) Ruan, L.; Ramezani-Dakhel, H.; Chiu, C.-Y.; Zhu, E.; Li, Y.; Heinz, H.; Huang, Y. *Nano Lett.* **2013**, *13*, 840. (e) Liu, X.; Yu, M.; Kim, H.; Mameli, M.; Stellacci, F. *Nat. Commun.* **2012**, *3*, 1182.

(7) (a) Ortiz, N.; Skrabalak, S. E. *Langmuir* **2014**, *30*, 6649. (b) Xia, Y.; Xia, X.; Peng, H.-C. *J. Am. Chem. Soc.* **2015**, *137*, 7947.

(8) (a) Berti, L.; Burley, G. A. *Nat. Nanotechnol.* **2008**, *3*, 81. (b) Lim, D.-K.; Jeon, K.-S.; Hwang, J.-H.; Kim, H.; Kwon, S.; Suh, Y. D.; Nam, J.-M. *Nat. Nanotechnol.* **2011**, *6*, 452. (c) Shen, J.; Xu, L.; Wang, C.; Pei, H.; Tai, R.; Song, S.; Huang, Q.; Fan, C.; Chen, G. *Angew. Chem., Int. Ed.* **2014**, *53*, 8338. (d) Zhang, F.; Nangreave, J.; Liu, Y.; Yan, H. *J. Am. Chem. Soc.* **2014**, *136*, 11198. (e) Jones, M. R.; Seeman, N. C.; Mirkin, C. A. *Science* **2015**, *347*, 1260901 DOI: 10.1126/science.1260901. (f) Zheng, J.; Nicovich, P. R.; Dickson, R. M. *Annu. Rev. Phys. Chem.* **2007**, *58*, 409. (g) Zheng, J.; Birktoft, J. J.; Chen, Y.; Wang, T.; Sha, R.; Constantinou, P. E.; Ginell, S. L.; Mao, C.; Seeman, N. C. *Nature* **2009**, *461*, 74. (h) Park, S. Y.; Lytton-Jean, A. K. R.; Lee, B.; Weigand, S.; Schatz, G. C.; Mirkin, C. A. *Nature* **2008**, *451*, 553. (i) Nykypanchuk, D.; Maye, M. M.; van der Lelie, D.; Gang, O. *Nature* **2008**, *451*, 549. (j) Tan, L. H.; Xing, H.; Chen, H.; Lu, Y. *J. Am. Chem. Soc.* **2013**, *135*, 17675−17678.

(9) (a) Demers, L. M.; Östblom, M.; Zhang, H.; Jang, N.-H.; Liedberg, B.; Mirkin, C. A. *J. Am. Chem. Soc.* **2002**, *124*, 11248. (b) Kimura-Suda, H.; Petrovykh, D. Y.; Tarlov, M. J.; Whitman, L. J. *J. Am. Chem. Soc.* **2003**, *125*, 9014. (c) Erdmann, M.; David, R.; Fornof, A. R.; Gaub, H. E. *Nat. Chem.* **2010**, *2*, 745.

(10) (a) Richards, C. I.; Choi, S.; Hsiang, J.-C.; Antoku, Y.; Vosch, T.; Bongiorno, A.; Tzeng, Y.-L.; Dickson, R. M. *J. Am. Chem. Soc.* **2008**, *130*, 5038. (b) Choi, S.; Dickson, R. M.; Yu, J. *Chem. Soc. Rev.* **2012**, *41*, 1867. (c) Petty, J. T.; Zheng, J.; Hud, N. V.; Dickson, R. M. *J. Am. Chem. Soc.* **2004**, *126*, 5207.

(11) (a) Hinds, S.; Taft, B. J.; Levina, L.; Sukhovatkin, V.; Dooley, C. J.; Roy, M. D.; MacNeil, D. D.; Sargent, E. H.; Kelley, S. O. *J. Am. Chem. Soc.* **2006**, *128*, 64. (b) Tikhomirov, G.; Hoogland, S.; Lee, P. E.; Fischer, A.; Sargent, E. H.; Kelley, S. O. *Nat. Nanotechnol.* **2011**, *6*, 485. (c) Cha, T.-G.; Baker, B. A.; Salgado, J.; Bates, C. J.; Chen, K. H.; Chang, A. C.; Akatay, M. C.; Han, J.-H.; Strano, M. S.; Choi, J. H. *ACS Nano* **2012**, *6*, 8136. (d) Deng, Z.; Samanta, A.; Nangreave, J.; Yan, H.; Liu, Y. *J. Am. Chem. Soc.* **2012**, *134*, 17424.

(12) Chen, Y.-C.; Wen, C.-C.; Liau, I.; Hsieh, Y.-Z.; Hsu, H.-Y. *J. Mater. Chem. B* **2014**, *2*, 4100.

(13) (a) Wang, Z.; Zhang, J.; Ekman, J. M.; Kenis, P. J. A.; Lu, Y. *Nano Lett.* **2010**, *10*, 1886. (b) Wang, Z.; Tang, L.; Tan, L. H.; Li, J.; Lu, Y. *Angew. Chem., Int. Ed.* **2012**, *51*, 9078. (c) Wu, J.; Tan, L. H.; Hwang, K.; Xing, H.; Wu, P.; Li, W.; Lu, Y. *J. Am. Chem. Soc.* **2014**, *136*, 15195. (d) Song, T.; Tang, L.; Tan, L. H.; Wang, X.; Satyavolu, N. S. R.; Xing, H.; Wang, Z.; Li, J.; Liang, H.; Lu, Y. *Angew. Chem., Int. Ed.* **2015**, *54*, 8114.

(14) (a) Alloyeau, D.; Dachraoui, W.; Javed, Y.; Belkahla, H.; Wang, G.; Lecoq, H.; Ammar, S.; Ersen, O.; Wisnet, A.; Gazeau, F.; Ricolleau, C. *Nano Lett.* **2015**, *15*, 2574. (b) Park, J. H.; Schneider, N. M.; Grogan, J. M.; Reuter, M. C.; Bau, H. H.; Kodambaka, S.; Ross, F. M. *Nano Lett.* **2015**, *15*, 5314.

(15) Millstone, J. E.; Wei, W.; Jones, M. R.; Yoo, H.; Mirkin, C. A. *Nano Lett.* **2008**, *8*, 2526.

(16) Burge, S.; Parkinson, G. N.; Hazel, P.; Todd, A. K.; Neidle, S. *Nucleic Acids Res.* **2006**, *34*, 5402.

(17) Jain, P. K.; Lee, K. S.; El-Sayed, I. H.; El-Sayed, M. A. *J. Phys. Chem. B* **2006**, *110*, 7238.

(18) Jin, R.; Charles Cao, Y.; Hao, E.; Metraux, G. S.; Schatz, G. C.; Mirkin, C. A. *Nature* **2003**, *425*, 487.

(19) Germain, V.; Li, J.; Ingert, D.; Wang, Z. L.; Pileni, M. P. *J. Phys. Chem. B* **2003**, *107*, 8717.

(20) Lofton, C.; Sigmund, W. *Adv. Funct. Mater.* **2005**, *15*, 1197.

(21) Hamilton, D. R.; Seidensticker, R. G. *J. Appl. Phys.* **1960**, *31*, 1165.

(22) Liao, H.-G.; Zherebetskyy, D.; Xin, H.; Czarnik, C.; Ercius, P.; Elmlund, H.; Pan, M.; Wang, L.-W.; Zheng, H. *Science* **2014**, *345*, 916.

(23) Wang, Z.; Bharathi, M. S.; Hariharaputran, R.; Xing, H.; Tang, L.; Li, J.; Zhang, Y.-W.; Lu, Y. *ACS Nano* **2013**, *7*, 2258.

(24) Rapino, S.; Zerbetto, F. *Langmuir* **2005**, *21*, 2512.

(25) Wang, Y.; He, J.; Liu, C.; Chong, W. H.; Chen, H. *Angew. Chem., Int. Ed.* **2015**, *54*, 2022.

DOI: 10.1021/jacs.5b09567
J. Am. Chem. Soc. 2015, 137, 14456−14464